ACS Catalysis

pubs.acs.org/acscatalysis Research Article

Controlled Manufacture of Heterogeneous Catalysts for the Hydrogenation of CO_2 via Steam Pyrolysis of Different Metal−Organic Frameworks

Il Son Khan, Luis Garzon-Tovar, Toni Grell, Genrikh Shterk, Jose Cerrillo, Tuiana Shoinkhorova, Juan C. Navarro, Faisal Alahmadi, Angel Sousa, Anastasiya Bavykina, Daria Poloneeva, Mustafa Caglayan, Stephanie Terruzzi, Javier Ruiz-Martinez, Nikolay Kosinov, Valentina Colombo, and Jorge Gascon*

Cite This: *ACS Catal.* 2023, 13, 1804−1811 Read Online

ACCESS | Metrics & More | Article Recommendations | Supporting Information

ABSTRACT: The use of metal−organic frameworks (MOFs) as precursors for the manufacture of heterogeneous catalysts has gained a great deal of attention over the last decade. By subjecting a given MOF to pyrolysis, electrochemical degradation, or other treatments under a controlled atmosphere, (supported) metal (oxide) nanoparticles with very narrow size distributions can be obtained, opening the door to the design of more efficient catalytic solids. Here, we demonstrate the benefits of steam during the controlled decomposition of two different MOF structures (Basolite F300(Fe) and In@ZIF-67(Co)) and the consequences of treatment under this mildly oxidizing atmosphere on the properties of the resulting catalysts for the direct hydrogenation of CO_2 to hydrocarbons and methanol. In-depth characterization demonstrates that steam addition helps to control the phase composition both before and after catalysis; additionally, it results in the formation of smaller nanoparticles, thus leading to more efficient catalysts in comparison with conventional pyrolysis.

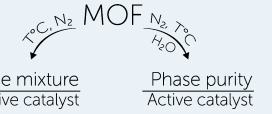

KEYWORDS: *MOF, CO_2 hydrogenation, MOF-mediated, pyrolysis, steam, steam-pyrolysis*

1. INTRODUCTION

Since their discovery, metal−organic frameworks (MOFs) have been proposed for multiple applications.[1−4] Their high porosity and crystallinity also offer additional possibilities. When thermally treated under controlled conditions, MOFs can be transformed into supported metal (oxide) nanoparticles (MNPs) with unusually uniform size distributions, even at very high metal loadings. This MOF-mediated synthesis (MOFMS) has been the focus of extensive research, as it allows one to obtain MNP-based solids that would be challenging (if not impossible) to obtain following conventional synthesis approaches where a higher content of MNPs results in agglomeration and thus a reduced metal dispersion.[5,6]

The key to this process is that during thermal decomposition under an inert atmosphere, the organic linkers decompose, forming a protective carbon layer around the MNP formed by the metal nodes of the MOF. Besides the access to highly loaded and dispersed systems, the pyrolysis of MOFs has also been shown to enable the synthesis of metal oxides with stoichiometries inaccessible through other synthetic routes.[7] The outcome of the pyrolysis depends sensitively on the conditions of the process. The pyrolysis temperature affects the formation of different carbon species. If too high, the formed carbon matrix can completely cover the metal nanoparticles. Temperatures that are too low, on the other hand, lead to the formation of heterogeneous carbon species and an incomplete reduction of the metal.[8]

Besides the pyrolysis temperature, the nature of the MOF's metal node plays a significant role too. With the help of the Ellingham diagram (plot of Gibbs free energy of oxides versus temperature), it is possible to determine the ease of reducing an oxide to its metallic form in the presence of a reducing agent. During MOF pyrolysis, the resulting carbon matrix acts as a reducing agent, where the intersection of its oxidation line with the metal oxidation line determines the temperature in which the carbon can reduce the metal oxide in the Ellingham diagram.[6] Metal reduction potentials above −0.27 V generally lead to the formation of metal nanoparticles, while potentials below this value lead to the formation of metal oxides instead.[9] However, there are exceptions to this rule. For instance, the composition of the final product resulting from the pyrolysis of iron-based MOFs depends mainly on the pyrolysis temperature and the nature of the parent MOF rather than the Fe^{3+} reduction potential. For example, for Basolite F300 (Fe-BTC), a MOF based on iron and trimesic acid (BTC), it was found that the composition can be tuned by varying the temperature. Pyrolysis performed between 400 and 700 °C results in the formation of Fe_3O_4 and θ-Fe_3C (cementite). At

Received: November 14, 2022
Revised: January 5, 2023

https://doi.org/10.1021/acscatal.2c05580
ACS Catal. 2023, 13, 1804−1811

900 °C, however, a larger amount of cementite particles is formed.[10] In contrast for Fe-MIL-127, θ-Fe_3C was obtained as the major product when the pyrolysis was performed between 400 and 700 °C.[11] Bimetallic systems with different reduction potentials are more complex; for instance, the pyrolysis of the bimetallic indium-cobalt systems leads to the formation of the bimetallic carbide phase $Co_3InC_{0.75}$ instead of a mixture of Co nanoparticles (NPs) and In_2O_3.[12,13]

In catalysis, where even small amounts of undesired phases can drastically influence the product distribution of the reaction, a precise control of catalyst composition is highly demanded. Therefore, even though in some examples the phase composition of the product can be influenced by varying temperature, phase purity and the desired composition cannot always be achieved by traditional pyrolysis under an inert atmosphere.

Herein, we explore the influence of steam during the pyrolysis process (steam pyrolysis) with the aim of gaining further control over the nature of the active species. Our results on two different MOFs, an iron-based MOF (Basolite F300) and a bimetallic indium-cobalt system based on indium impregnated MOF (In@ZIF-67(Co)), demonstrate that steam pyrolysis contributes to decreasing the average particle size and to formation of a more porous carbon matrix around metal particles. These changes have large implications for catalytic performance.

2. MATERIALS AND METHODS

2.1. Material Preparation. *2.1.1. Synthesis of ZIF-67.* To synthesize ZIF-67, two solutions of precursors were prepared. First, 3.59 g (12 mmol) of $Co(NO_3)_2{\cdot}6H_2O$ was dissolved in 250 mL of MeOH. Second, 8.11 g (99 mmol) of 2-methylimidazole was dissolved in 250 mL of MeOH. The first solution was poured into the second solution, and the resulting mixture was stirred for 12 min and left overnight under ambient conditions without stirring.[14] The obtained product was collected by centrifugation and washed with MeOH three times. The solid was dried overnight at 70 °C. Ultimately, the solid was activated in a vacuum oven overnight at 130 °C under 30 inHg vacuum.

2.1.2. Synthesis of ZIF-67(In). Activated powder of ZIF-67 was impregnated with indium nitrate according to a slightly modified reported procedure.[13] Then, 1 g of ZIF-67 was impregnated with 0.498 g of indium nitrate dissolved in 1 mL of water. The obtained slurry was dried in an oven overnight at 70 °C.

2.1.3. Synthesis of M@C (M = Fe, In−Co) Materials. The carbonization of Basolite F300 and ZIF-67(In) was conducted in a quartz tubular reactor vertically placed in a tube furnace. In a typical experiment, MOF powder was placed in the reactor under continuous N_2 flow (25 mL min^{-1}) followed by direct carbonization at different temperatures (600 and 800 °C) for 6 or 2 h using a heating ramp of 2 or 5 °C min^{-1}. After cooling down of the reactor, the samples were passivated in continuous flow of N_2 (25 mL min^{-1}) and air (5 mL min^{-1}) for 2 h.

2.1.4. Potassium Impregnation of Fe@C Samples. Fe@C samples were impregnated with a solution of K_2CO_3 in water by incipient wetness impregnation to achieve a K content of 2 wt %.

2.1.5. Steam Pyrolysis. In a typical experiment, a water bubbler was connected to a nitrogen line. The water content was controlled by varying the temperature of the water cooler connected to the bubbler (5, 25, and 40 °C). The MOF powder was placed in the reactor under a continuous wet flow of N_2 (25 mL min^{-1}) at different temperatures (600 and 800 °C) for 6 or 2 h using a heating ramp of 2 °C min^{-1} or 5 °C min^{-1} (Scheme S1).

2.2. Catalyst Characterization. Powder X-ray diffraction (PXRD) analyses were carried out using a Bruker D8 Advanced diffractometer in Bragg−Brentano geometry fitted with a copper tube operating at 40 kV and 40 mA. The diffractograms were acquired over the 2θ range of 10−90°, using a step size of 0.018° with a time per step of 8 s. The crystalline phases were identified by comparison data from the Powder Diffraction File PDF-4.[15] Whole powder pattern refinements were carried out adopting the Le Bail method,[16] as implemented in TOPAS V6.[17] Rietveld refinements were performed with the same software, starting from the crystal structures deposited in the NIST Inorganic Crystal Structure Database (ICSD).[18]

N_2 adsorption−desorption measurements were done at 77 K using a Micromeritics ASAP 2040 instrument. Before the measurements, Fe@C and In-Co@C samples were degassed at 120 °C for 12 h and at 180 °C for 16 h under vacuum, respectively.

Raman experiments were conducted using a confocal Raman microscope WITec Apyron equipped with a 473 nm laser and power of 1.0 mW. An oil immersion objective (Zeiss Achroplan/N-Achroplan Oil 100×/NA 1.25) and immersion oil (Immersol, Carl Zeiss) were applied in all acquisitions to collect the Raman spectra with an integration time of 20 s and accumulation number of 5. Raman spectra from different locations were collected for each sample.

Inductively coupled plasma (ICP) analysis was carried out in a 5100 ICP-OES instrument (Agilent) and SPS 4 Autosampler (Agilent) with Ar being used as a gas supply. Digestion was done at max 240 °C and max 35 bar using an UltraWAVE apparatus (Milestone) with Aqua regia for MOFs and Aqua regia + HF solution for carbonized samples. Prior to digestion of the samples, the vessel cleaning step was performed using only nitric acid (5 mL). A calibration curve (4 plots) was built (1−10−25−100 ppm), and all samples were duplicated. Moreover, laboratory reagent blank, laboratory fortified blank, quality control sample, and continuing calibration verification samples were recorded to validate the results as recommended in several standard methods.

Thermogravimetric data were collected under an air atmosphere using a Mettler-Toledo thermal analyzer at a heating rate of 5 °C min^{-1} in the temperature range of 25−900 °C and a gas flow of 25 mL min^{-1}.

X-ray photoelectron spectra (XPS) were recorded using a K-Alpha spectrometer (Thermo Scientific) with a monochromatic X-ray source (1486.68 eV, Al Kα anode operating at 72 W, spot size of 400 μm). Samples were placed on a double-sided carbon tape operating at 72 W with a spot size of 400 μm. The spectra were analyzed using the CasaXPS software (version 2.3.19).

Transmission electron microscopy (TEM) micrographs were obtained with a Titan ST microscope operated at an acceleration voltage of 300 kV. High-angle annular dark-field imaging measurements were performed on a Cs-Probe Corrected Titan microscope (Thermo-Fischer Scientific) equipped with a GIF Quantum (Gatan Inc.) and Super-X EDXS detectors (Thermo-Fischer Scientific). The images were acquired at the same acceleration voltage (300 kV). For the

https://doi.org/10.1021/acscatal.2c05580
ACS Catal. 2023, 13, 1804−1811

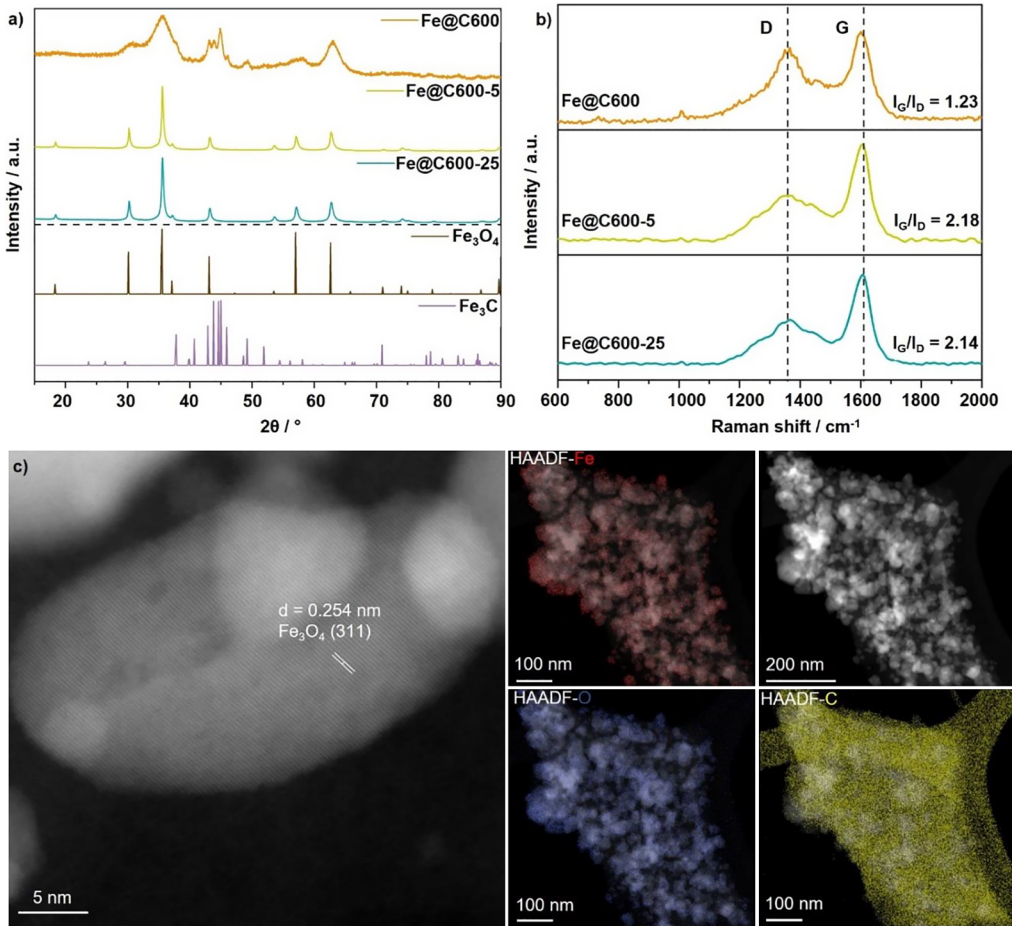

Figure 1. (a) Powder X-ray diffractograms for **Fe@C600** (orange), **Fe@C600-5** (yellow), and **Fe@C600-25** (turquoise) and simulated patterns for c-Fe_3O_4 (brown), Fe_3C (lavender) (for detailed Rietveld analysis, see the Supporting Information). (b) Raman spectra of **Fe@C600** (orange), **Fe@C600-5** (yellow), and **Fe@C600-25** (turquoise). Peaks located at 1360 and 1586 cm^{-1} are attributed to the vibration bands of carbon in disordered graphite (D band) and the E_{2g} mode of graphite (G band), respectively. (c) High-resolution dark-field STEM images of **Fe@C600-25** and STEM-EELS mapping showing the distribution of Fe, O, and C throughout the solid.

establishment of the particle size distribution, close to 200 particles from different micrographs were analyzed.

Scanning electron microscopy (SEM) images were recorded using a Zeiss Merlin instrument at a constant acceleration voltage of 8 kV.

2.3. CO_2 Hydrogenation Tests. Catalytic tests were executed in 4 channel Flowrence of Avantium. One mixed feed gas flow is distributed over 4 channels with a relative standard deviation of 2%. The mixed feed has 25 vol % of CO_2 and 75 vol % of H_2 or 20% CO_2 and 80% of H_2. In addition, 0.5 mL min^{-1} of He is mixed with the feed as the internal standard. The channels are stainless-steel tubes inserted in a furnace. The tubes have an outside diameter of 3 mm, an inside diameter of 2 mm, and a length of 300 mm. One of the 4th channels was always used without a catalyst as blank. The tubes are pressurized to 50 bar using a membrane-based pressure controller working with N_2 pressure.

The conversions (X, %) and selectivities (S, %) are defined as follows:

$$X_{CO_2} = \left(1 - \frac{C_{He,blk} \times C_{CO_2,R}}{C_{He,R} \times C_{CO_2,blk}}\right) \times 100 \quad (1)$$

$$S_{Cn} = \frac{n \times \left(\frac{C_{Cn,R}}{C_{He,R}}\right)}{\left(\frac{C_{CO_2,blk}}{C_{He,blk}} - \frac{C_{CO_2,R}}{C_{He,R}}\right)} \times 100 \quad (2)$$

3. RESULTS AND DISCUSSION

As the first system for the study, we chose Fe-based MOF Basolite F300 (Fe-BTC) as a template for the preparation of different solids under N_2 and N_2/H_2O flows. The carbonization of Fe-BTC was carried out at 600 °C for 6 h under a N_2 atmosphere. After this treatment, the resulting material was passivated at room temperature, using 2.5% (v/v) O_2 in N_2 for 2 h. This sample was denoted as **Fe@C600**. To control the partial pressure of steam (0.86 and 3.13%) during the steam pyrolysis, a bubbler at different temperatures (5 and 25 °C) was used (Scheme S1). These samples are denoted as **Fe@C600-5** and **Fe@C600-25** where the first number stands for the pyrolysis temperature and the second for the bubbler temperature. PXRD analysis revealed that the one and only crystalline phase formed during the steam pyrolysis is Fe_3O_4, which was confirmed by Rietveld refinement (Figure 1a), whereas during pyrolysis we observed a mixture of Fe_3O_4 and θ-Fe_3C (Figures S1−S3). We also noticed that for the steam-pyrolyzed samples (**Fe@C600-5,25**), the steam content does

https://doi.org/10.1021/acscatal.2c05580
ACS Catal. 2023, 13, 1804−1811

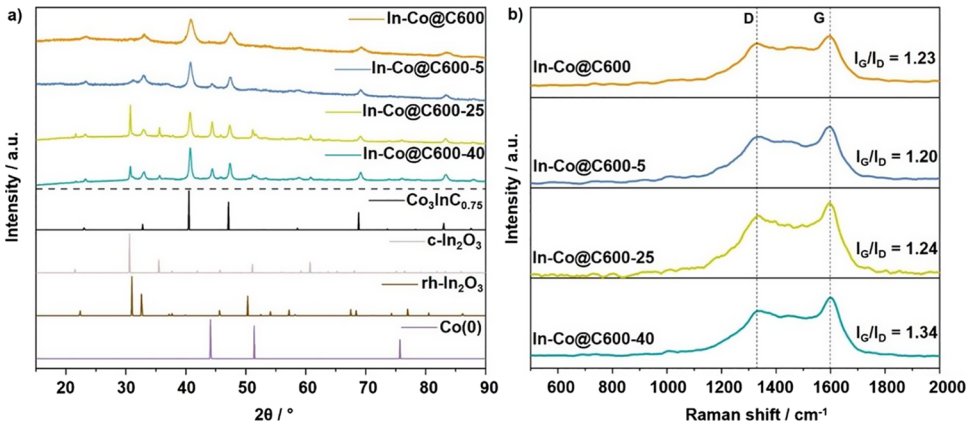

Figure 2. (a) Powder X-ray diffractograms for **In-Co@C600** (orange), **In-Co@C600-5** (blue), **In-Co@C600-25** (yellow), and **In-Co@C600-40** (turquoise) and simulated patterns for $Co_3InC_{0.75}$ (black), c-In_2O_3 (warm mid gray), rh-In_2O_3 (brown), and α-Co(0) (lavender) (for detailed Rietveld analysis, see the Supporting Information). (b) Raman spectra of **In-Co@C600** (orange), **In-Co@C600-5** (blue), **In-Co@C600-25** (yellow), and **In-Co@C600-40** (turquoise). Peaks located at 1360 and 1586 cm^{-1} are attributed to the vibration bands of carbon in disordered graphite (D band) and the E_{2g} mode of graphite (G band), respectively.

not influence the final phase composition. Even low water content leads to Fe_3O_4 as the only observed phase (Figure S2). We speculate that water acts as an oxidizing agent during pyrolysis, hampering the formation of θ-Fe_3C in the final material. It is also worth noting that the crystallinity of the steam-pyrolyzed samples is higher than that in the conventionally pyrolyzed samples. This aligns with the data reported for the previous experiment with water co-feeding during pyrolysis of ZIF-8.[19,20] We also found that at a higher steam-pyrolysis temperature (800 °C), only Fe_3O_4 was formed, in contrast to the resulting mixture of Fe_3O_4, FeC, θ-Fe_3C, and Fe(0) after pyrolysis under a N_2 atmosphere at the same temperature (see the Supporting Information).

We performed thermogravimetric analysis (TGA) of the resulting solids. TGA curves show mass losses of 42% (**Fe@C600**), 36% (**Fe@C600-5**), and 34% (**Fe@C600-25**) (Figure S4), confirming the partial gasification of carbon along with the absence of carbidic species in the samples treated under steam. BET analyses are in line with TGA, showing a slight decrease in the specific surface areas with carbon content decreases of 265, 215, and 214 $m^2\ g^{-1}$ for the three different samples (Figure S5). The second key parameter of the resulting carbon matrix is its graphitization degree, which was studied by Raman spectroscopy. The Raman spectra of the materials exhibit the characteristic vibration bands of disordered graphite (D band) at 1360 cm^{-1} and the E_{2g} mode of graphite (G band) at 1586 cm^{-1}. The intensity ratio of the two bands (I_G/I_D) was used to evaluate the graphitization degree of the different solids. Thus, we found that the addition of water during pyrolysis leads to a higher graphitization degree of the carbon matrix (2.18 for **Fe@C600-5** and 2.14 for **Fe@C600-25**) than that obtained for **Fe@C600** (1.23) as it is shown in Figure 1b. These data are in accordance with the decrease of the BET values for **Fe@C600-5** and **Fe@C600-25** in comparison with **Fe@C600**. The higher weight loss for **Fe@C600** during TGA suggests that the addition of water partially removes amorphous carbon from the samples similar to the steam decoking process, resulting in a higher graphitization of carbon and a higher overall crystallinity of the samples.

The surface analysis of **Fe@C600-*X*** by XPS showed that for the steam-pyrolyzed samples, the surface content of Fe(0) decreases from 4.4% for **Fe@C600** to 0.5 and 0.3% for **Fe@C600-5** and **Fe@C600-25**, respectively (Table S1). This is in accordance with the PXRD analysis in which no Fe(0) species were detected for the bulk material. XPS revealed that the surface iron of all the samples consists of Fe^0, Fe^{2+}, and Fe^{3+} species (Figure S6). The O 1s core level spectra were deconvoluted into three peaks located at 529.9, 531.7, and 533.2 eV corresponding to the M−O−M, M−OH, and M−H_2O/C=O bonds, respectively (Figure S7). The C 1s spectra were fitted with four components located at 284.4, 286.0, 288.6, 288.3, and 290.8 eV corresponding to the adventitious carbon, carbon tape, and C=C(sp2); C−O−C and C−C (sp3); O=C−OH; and CO_3^{2-}, respectively (Figure S8). The same oxygen and carbon species were found for both pyrolyzed and steam-pyrolyzed samples.

TEM imaging of the resulting materials confirms the formation of NPs confined within a graphitic carbon matrix with average particle sizes of 5.69 ± 6.16 (**Fe@C600**), 4.92 ± 3.47 (**Fe@C600-5**), and 2.86 ± 1.73 nm (**Fe@C600-25**) (Figures 1c, S9−S11). Interestingly, as the water content increases, the particle size of the resulting materials decreases.

SEM images showed no difference in the microstructure of the resulting materials with and without steam (Figures S12−S14).

To understand if this procedure is also applicable to other Fe-based MOFs, we performed the steam pyrolysis of **Fe-MIL-88B** (Figure S15) and **Fe-MIL-127** (Figure S16) under similar conditions to those of **Fe@C600-25**. PXRD patterns of the resulting materials showed that Fe_3O_4 was obtained as a unique phase (Figure S17). This demonstrates that the phase composition can be controlled for Fe-based MOFs using our approach independently of the pyrolysis temperature or nature of the parent MOF.

We now shift our attention toward the more complex bimetallic indium−cobalt case. This system is particularly interesting since it was used as a precursor to prepare a methanol-producing catalyst.[21] However, the pyrolysis of **In@ZIF-67(Co)** leads to the predominant formation of inactive $Co_3InC_{0.75}$. In fact, PXRD and extended X-ray absorption fine structure analyses revealed that the active phase composition of the catalyst consists of a mixture of $Co_3InC_{0.75}$, α-Co, cubic polymorph of In_2O_3 (c-In_2O_3), and traces of rhombohedral In_2O_3 phase (rh-In_2O_3).[13] However, to achieve this mixture, a

https://doi.org/10.1021/acscatal.2c05580
ACS Catal. 2023, 13, 1804−1811

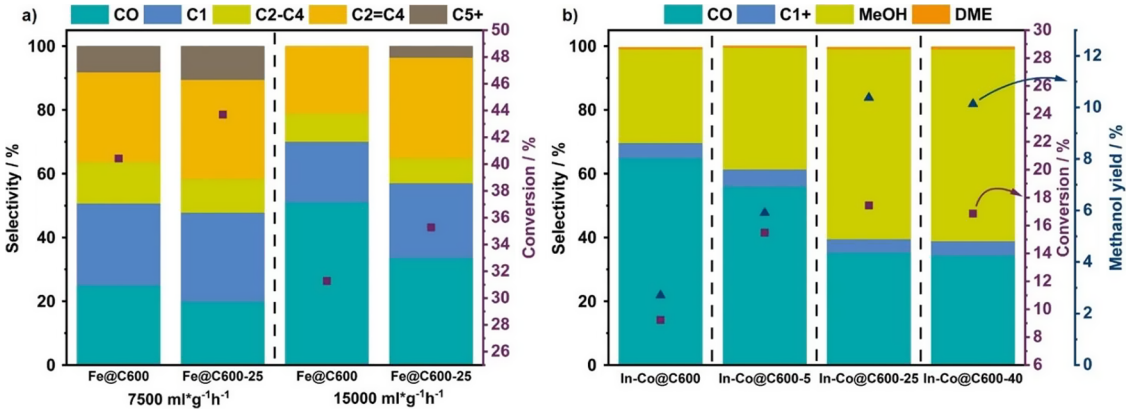

Figure 3. (a) CO_2 conversion and selectivity to hydrocarbons of **Fe@C600** and **Fe@C600-25** in CO_2 hydrogenation reaction. Reaction conditions: 350 °C, 50 bar, H_2/CO_2 = 3, and GHSV of 7500 and 15,000 mL g^{-1} h^{-1}. (b) CO_2 conversion, selectivity, and yield methanol of **In-Co@C600**, **In-Co@C600-5**, **In-Co@C600-25**, and **In-Co@C600-40**. Reaction conditions: 300 °C, 50 bar, H_2/CO_2 = 4, and GHSV of 22,500 mL g^{-1} h^{-1}. *"Cn" stands for the hydrocarbon fraction, hyphen for paraffins, and equal sign for olefins.

three-step procedure is required (pyrolysis, calcination, and activation). We, therefore, hypothesized that the presence of water during the pyrolysis of In@ZIF-67(Co) could lead to the formation of the active mixture in a single step.

In order to confirm this hypothesis, we impregnated ZIF-67 with indium using a slightly modified version of the reported procedure (see the Experimental Section, Figure S18).[13]

After impregnation, ICP-MS analysis showed an In/Co mass ratio of 5:9 (0.56), while in the reported procedure, the ratio was 3:8 (0.375). In good agreement with our previous data, PXRD analysis of the sample obtained in a pure nitrogen atmosphere (**In-Co@C600**) revealed the formation of $Co_3InC_{0.75}$ as the predominant phase and the minor formation of rh-In_2O_3 and Co(0) (Figure S19). At a lower water content (0.86%) in the N_2 flow, the PXRD results of **In-Co@C600-5** showed that the reflections of rh-In_2O_3 and cobalt NPs become more intense, indicating higher content of those phases, which is in line with what we observed above for the Fe samples (Figure S20).

Interestingly, reflections of c-In_2O_3 appear in the PXRD patterns of **In-Co@C600-25** (3.13%) and **In-Co@C600-40** (7.28%), demonstrating that the increase of water content promotes the formation of c-In_2O_3 alongside with rh-In_2O_3 (Figures S21 and S22). In good agreement with our hypothesis, we observed that the presence of water allows the formation of the four main phases (c-In_2O_3, $Co_3InC_{0.75}$, Co NPs, and rh-In_2O_3) that are the active components of the methanol-producing catalyst.[21] In this example, as for the steam-pyrolyzed samples of Basolite F300, a higher crystallinity was observed compared to the conventional pyrolysis product (Figure 2a).

TGA for these samples showed weight losses of 45% for **In-Co@C600**, 33% for **In-Co@C600-5**, 9% for **In-Co@C600-25**, and 20% for **In-Co@C600-40** (Figure S23). The difference in mass loss observed during the TGA for **In-Co@C600-25** and **In-Co@C600-40** is based on the phase composition of these samples. We observed a higher weight loss in the case of **In-Co@C600-40** due to the simultaneous higher amount of $Co_3InC_{0.75}$ and lower amount of In_2O_3 phases than in **In-Co@C600-25**. This happens due to the following. During the TGA under an oxidative atmosphere $Co_3InC_{0.75}$ forms Co_3O_4 and In_2O_3, Co(0) is transformed into Co_3O_4, and In_2O_3 stays intact. As the compositions of both In@ZIF-67 materials before steam pyrolysis were the same, more In_2O_3 observed after pyrolysis means a lower weight loss during TGA. The difference in the content of $Co_3InC_{0.75}$ in **In-Co@C600-25** and **In-Co@C600-40** can be explained by a higher degree of graphitization of the carbon matrix. Raman spectroscopy showed a higher degree of graphitization for the samples pyrolyzed under higher steam partial pressures (I_G/I_D ratios of 1.23 for **In-Co@C600**, 1.20 for **In-Co@C600-5**, 1.24 for **In-Co@C600-25**, and 1.34 for **In-Co@C600-40**) (Figure 3b). This is the result of a higher steam content in the gas flow. In fact, another synthetic method of this bimetallic carbide is based on the direct carburization of In and Co sources with graphite.[22] BET analysis for the samples showed that surface area increases with the partial pressure of steam applied. As such **In-Co@C600** showed hardly any porosity while BET surface areas of 136, 121, and 154 m^2 g^{-1} were found for **In-Co@C600-5**, **In-Co@C600-25**, and **In-Co@C600-40**, respectively (Figure S24). Notably, this system shows the opposite trend compared to the **Fe@C** samples.

XPS data (Figures S25−S29) showed an increasing amount of Co(0) with steam partial pressure: 1.89%(**In-Co@C600-5**), 2.84%(**In-Co@C600-25**), and 3.84%(**In-Co@C600-40**) (Table S2), along with a simultaneous increase of indium oxide content, in agreement with the PXRD analysis. Altogether, these results suggest that steam pyrolysis prevents, to a large extent, the formation of the undesired $Co_3InC_{0.75}$ phase. For the conventionally pyrolyzed sample **In-Co@C600**, the amount of Co(0) is 7.13%, present in the form of mixed carbide and MNP. XPS of **In-Co@C600-X** revealed that the surface Co exists in form of Co^0, Co^{2+}, and Co^{3+} (Figure S25). Indium components at $3d_{3/2}$ and $3d_{5/2}$ were fitted with single components of In_2O_3, the binding energy of **In-Co@C600-*X*** (*X* = 5, 25, 40) is 444.5 eV, and in the case of **In-Co@C600**, it is 445.0 eV. This shift can be explained by the presence of In−Co mixed oxide after steam pyrolysis (Figure S26).[23]

TEM images of the resulting materials confirmed the formation of NPs confined within a graphitic carbon matrix with average particle sizes of 9.08 ± 4.39 (**In-Co@C600**), 5.86 ± 2.60 (**In-Co@C600-5**), 6.21 ± 2.76 (**In-Co@C600-25**), and 13.27 ± 6.45 nm (**In-Co@C600-40**) (Figures S30−S33). The most significant detail here is that with addition of small water quantities, i.e., 0.86% (**In-Co@C600-5**) and 3.13% (**In-Co@C600-25**) in the nitrogen flow, the average particle size

https://doi.org/10.1021/acscatal.2c05580
ACS Catal. 2023, 13, 1804−1811

decreases in comparison with conventional pyrolysis. However, a higher water content of 7.28% results in a jump of the average particle size.

As in the case of **Fe@C** samples, SEM imaging did not show any difference in the microstructure of the resulting solids with and without water addition (Figures S34−37).

To prove the concept that the method investigated here leads to significant changes in catalytic performance, we conducted CO_2 hydrogenation tests using both MOF-mediated systems. The performance of iron-based MOFMSs was evaluated in the catalytic CO_2 hydrogenation to hydrocarbons, while the In−Co system was tested in the direct production of methanol from CO_2.

After pyrolysis, the iron samples **Fe@C600** and **Fe@C600-25** were impregnated with 2 wt % of potassium, to promote their CO_2 hydrogenation catalytic performance. The presence of this alkali metal ion favors CO_2 adsorption and olefin production, improving not only conversion but also the olefin-to-paraffin ratio.[24−26] Before the catalytic tests, temperature-programmed reduction (TPR) analysis of both impregnated samples was performed to study the reducibility of the catalysts. H_2-TPR profiles of the materials showed a similar behavior, a first hydrogen consumption peak from ∼300 to 500 °C corresponding to the reduction of Fe_3O_4 to FeO and the one at ∼600 °C associated with the reduction of FeO to Fe(0) and the decomposition of the carbon matrix (Figure S38).[27] Based on these results, **Fe@C600** and **Fe@C600-25** were pretreated at 350 °C under a hydrogen atmosphere for 4 h before the catalytic studies. The iron catalysts were tested in the CO_2 hydrogenation reaction at 350 °C, 50 bar, H_2/CO_2 = 3, and two different gas hourly space velocities (GHSVs), 7500 and 15,000 mL g^{-1} h^{-1}. The catalytic results (Figure 3a) showed a decrease in the conversion and a different product distribution when GHSV was increased for both Fe-catalysts. Based on the previous work published by our group,[28,29] the mechanism for the CO_2 hydrogenation to hydrocarbons on Fe systems is based on the transformation of CO_2 to CO by reverse water gas shift reaction and the subsequent transformation of the CO into hydrocarbons via a Fischer−Tropsch reaction pathway. Therefore, the increase of CO formation and decrease of hydrocarbon products, especially C_5^+, observed at a higher GHSV happen due to the reduced contact time, which impedes the transformation of the initially produced CO to hydrocarbons.

If we compare the performance of both catalysts under the same reaction conditions, the steam-pyrolyzed MOF (**Fe@600-25**) always achieves a higher conversion at any GHSV with a product distribution showing less CO and a higher yield to hydrocarbons. This improvement is attributed not only to the different phase composition of the systems but also to the fact that **Fe@600-25** presents a smaller particle size and higher crystallinity of the Fe_3O_4 phase (Table S3). Liu et al. speculated that an appropriate ratio between Fe_3O_4 and Fe_5C_2 (Hägg carbide) is necessary to achieve the best performance in CO_2 hydrogenation.[26] Indeed, PXRD analysis of **Fe@C600** and **Fe@C600-25** after catalysis revealed different ratios for the two solids: $(Fe_5C_2 + Fe_7C_3)/Fe_3O_4$ = 1.3 for **Fe@C600-25** and 0.9 for **Fe@C600** (Figures S39 and S40).

Subsequently, the In@ZIF-67(Co)-mediated catalysts were tested in the CO_2 hydrogenation to methanol at 300 °C, 50 bar, a H_2/CO_2 ratio of 4, and a GHSV of 22,500 mL g^{-1} h^{-1}.

Among all the solids, **In-Co@C600-25** and **In-Co@C600-40** displayed the highest activity. These catalysts showed a methanol yield higher than 10%. The conventionally pyrolyzed MOF (**In-Co@C600**) showed the lowest methanol yield, ∼3%. This significant difference in the catalytic activity correlates with the different phase composition of the samples and particle size of the material (Table S4), as discussed above (Figure 3b). The most active catalysts are the ones presenting the c-In_2O_3 phase along with $Co_3InC_{0.75}$, rh-In_2O_3, and Co^0. All these species play different roles in the mechanism, but, particularly, the presence of c-In_2O_3 enhances catalytic activity compared to rh-In_2O_3, due to its higher reducibility and reactivity.[30,31] Consequently, **In-Co@C600-25** and **In-Co@C600-40** reach higher CO_2 conversions (17%) with no significant differences between them. In the same line, the **In-Co@C600-5** and the conventionally pyrolyzed **In-Co@C600** samples, neither of which possess the c-In_2O_3 phase, show lower activities. Furthermore, the immediate presence of these phases within the steam-pyrolyzed samples leads to the absence of the classical induction/activation period of 10−30 h found for this family of catalysts.[21]

4. CONCLUSIONS

In summary, the addition of steam during MOF pyrolysis allows for further control of the resulting materials and their catalytic performance. The presence of steam under pyrolysis conditions preserves the main benefits of pyrolysis but allows for additional control over the obtained metal(oxide) and carbon phases. In the two examples presented here, this resulted in superior catalytic performance. In the case of Basolite F300, steam pyrolysis prevents, to a large extent, the formation of cementite while reducing the average particle size of the metal species. As a result, more active and selective catalysts for the synthesis of olefins from CO_2 were manufactured. In the case of In@ZIF-67(Co), the formation of mixed metal carbidic species can be avoided, enhancing in this way catalyst activity and selectivity for methanol in the direct hydrogenation of CO_2. We expect that this approach will be useful not only for the MOFs and the application studied here but for many other catalytic processes.

■ ASSOCIATED CONTENT

Supporting Information

The Supporting Information is available free of charge at https://pubs.acs.org/doi/10.1021/acscatal.2c05580.

Experimental details, synthetic procedures, Rietveld refinement plots, TGA and DTG curves, N_2 adsorption isotherms and BET fits, XPS spectra and data, TEM and EELS mapping images, particle size distribution histograms, PXRD diffractograms, and H_2-TPR data (PDF)

■ AUTHOR INFORMATION

Corresponding Author

Jorge Gascon − *Advanced Catalytic Materials (ACM), KAUST Catalysis Center (KCC), King Abdullah University of Science and Technology (KAUST), Thuwal 23955-6900, Saudi Arabia;* orcid.org/0000-0001-7558-7123; Email: jorge.gascon@kaust.edu.sa

Authors

Il Son Khan − *Advanced Catalytic Materials (ACM), KAUST Catalysis Center (KCC), King Abdullah University of Science*

https://doi.org/10.1021/acscatal.2c05580
ACS Catal. 2023, 13, 1804−1811

and Technology (KAUST), Thuwal 23955-6900, Saudi Arabia; orcid.org/0000-0003-0549-1737

Luis Garzon-Tovar − *Advanced Catalytic Materials (ACM), KAUST Catalysis Center (KCC), King Abdullah University of Science and Technology (KAUST), Thuwal 23955-6900, Saudi Arabia;* orcid.org/0000-0003-0253-4041

Toni Grell − *Dipartimento di Chimica, Università degli Studi di Milano, Milan 20133, Italy;* orcid.org/0000-0001-9162-6487

Genrikh Shterk − *Advanced Catalytic Materials (ACM), KAUST Catalysis Center (KCC), King Abdullah University of Science and Technology (KAUST), Thuwal 23955-6900, Saudi Arabia*

Jose Cerrillo − *KAUST Catalysis Center (KCC), King Abdullah University of Science and Technology, Thuwal 23955-6900, Saudi Arabia;* orcid.org/0000-0001-8824-8294

Tuiana Shoinkhorova − *Advanced Catalytic Materials (ACM), KAUST Catalysis Center (KCC), King Abdullah University of Science and Technology (KAUST), Thuwal 23955-6900, Saudi Arabia;* orcid.org/0000-0002-3571-9520

Juan C. Navarro − *KAUST Catalysis Center (KCC), King Abdullah University of Science and Technology, Thuwal 23955-6900, Saudi Arabia*

Faisal Alahmadi − *Advanced Catalytic Materials (ACM), KAUST Catalysis Center (KCC), King Abdullah University of Science and Technology (KAUST), Thuwal 23955-6900, Saudi Arabia*

Angel Sousa − *Advanced Catalytic Materials (ACM), KAUST Catalysis Center (KCC), King Abdullah University of Science and Technology (KAUST), Thuwal 23955-6900, Saudi Arabia*

Anastasiya Bavykina − *Advanced Catalytic Materials (ACM), KAUST Catalysis Center (KCC), King Abdullah University of Science and Technology (KAUST), Thuwal 23955-6900, Saudi Arabia;* orcid.org/0000-0003-3456-7358

Daria Poloneeva − *Advanced Catalytic Materials (ACM), KAUST Catalysis Center (KCC), King Abdullah University of Science and Technology (KAUST), Thuwal 23955-6900, Saudi Arabia*

Mustafa Caglayan − *Advanced Catalytic Materials (ACM), KAUST Catalysis Center (KCC), King Abdullah University of Science and Technology (KAUST), Thuwal 23955-6900, Saudi Arabia;* orcid.org/0000-0002-9359-0841

Stephanie Terruzzi − *Dipartimento di Chimica, Università degli Studi di Milano, Milan 20133, Italy;* orcid.org/0000-0003-4964-2891

Javier Ruiz-Martinez − *KAUST Catalysis Center (KCC), King Abdullah University of Science and Technology, Thuwal 23955-6900, Saudi Arabia;* orcid.org/0000-0002-9850-7939

Nikolay Kosinov − *Laboratory of Inorganic Materials and Catalysis, Department of Chemical Engineering and Chemistry, Eindhoven University of Technology, Eindhoven 5600 MB, The Netherlands;* orcid.org/0000-0001-8520-4886

Valentina Colombo − *Dipartimento di Chimica, Università degli Studi di Milano, Milan 20133, Italy; Consorzio Interuniversitario Nazionale per la Scienza e Tecnologia dei Materiali (INSTM), Firenze 50121, Italy;* orcid.org/0000-0003-0263-4456

Complete contact information is available at: https://pubs.acs.org/10.1021/acscatal.2c05580

Author Contributions

All authors have given approval to the final version of the manuscript.

Funding

Funding for this work was provided by King Abdullah University of Science and Technology (KAUST). V.C. thanks the Italian MUR for funding through the PRIN2017 program (project "Moscato" n° 2017KKP5ZR_004) and Università degli Studi di Milano for the Transition Grant (PSR2015-1721VCOLO_01).

Notes

The authors declare no competing financial interest.

■ ACKNOWLEDGMENTS

The authors wish to thank and acknowledge Dr. Samy Ould-Chikh for valuable scientific discussions.

■ REFERENCES

(1) Qian, Q.; Asinger, P. A.; Lee, M. J.; Han, G.; Mizrahi Rodriguez, K.; Lin, S.; Benedetti, F. M.; Wu, A. X.; Chi, W. S.; Smith, Z. P. MOF-Based Membranes for Gas Separations. *Chem. Rev.* **2020**, *120*, 8161−8266.

(2) Xie, L. S.; Skorupskii, G.; Dincă, M. Electrically Conductive Metal−Organic Frameworks. *Chem. Rev.* **2020**, *120*, 8536−8580.

(3) Lim, D.-W.; Kitagawa, H. Proton Transport in Metal−Organic Frameworks. *Chem. Rev.* **2020**, *120*, 8416−8467.

(4) Yang, J.; Yang, Y.-W. Metal−Organic Frameworks for Biomedical Applications. *Small* **2020**, *16*, No. 1906846.

(5) Wang, Q.; Astruc, D. State of the Art and Prospects in Metal−Organic Framework (MOF)-Based and MOF-Derived Nanocatalysis. *Chem. Rev.* **2020**, *120*, 1438−1511.

(6) Oar-Arteta, L.; Wezendonk, T.; Sun, X.; Kapteijn, F.; Gascon, J. Metal organic frameworks as precursors for the manufacture of advanced catalytic materials. *Mater. Chem. Front.* **2017**, *1*, 1709−1745.

(7) Castells-Gil, J.; Ould-Chikh, S.; Ramírez, A.; Ahmad, R.; Prieto, G.; Gómez, A. R.; Garzón-Tovar, L.; Telalovic, S.; Liu, L.; Genovese, A.; Padial, N. M.; Aguilar-Tapia, A.; Bordet, P.; Cavallo, L.; Martí-Gastaldo, C.; Gascon, J. Unlocking mixed oxides with unprecedented stoichiometries from heterometallic metal-organic frameworks for the catalytic hydrogenation of CO2. *Chem. Catal.* **2021**, *1*, 364−382.

(8) Khan, I. S.; Mateo, D.; Shterk, G.; Shoinkhorova, T.; Poloneeva, D.; Garzón-Tovar, L.; Gascon, J. An Efficient Metal−Organic Framework-Derived Nickel Catalyst for the Light Driven Methanation of CO2. *Angew. Chem., Int. Ed.* **2021**, *60*, 26476−26482.

(9) Das, R.; Pachfule, P.; Banerjee, R.; Poddar, P. Metal and metal oxide nanoparticle synthesis from metal organic frameworks (MOFs): finding the border of metal and metal oxides. *Nanoscale* **2012**, *4*, 591−599.

(10) Wezendonk, T. A.; Santos, V. P.; Nasalevich, M. A.; Warringa, Q. S. E.; Dugulan, A. I.; Chojecki, A.; Koeken, A. C. J.; Ruitenbeek, M.; Meima, G.; Islam, H.-U.; Sankar, G.; Makkee, M.; Kapteijn, F.; Gascon, J. Elucidating the Nature of Fe Species during Pyrolysis of the Fe-BTC MOF into Highly Active and Stable Fischer−Tropsch Catalysts. *ACS Catal.* **2016**, *6*, 3236−3247.

(11) Wezendonk, T. A.; Warringa, Q. S. E.; Santos, V. P.; Chojecki, A.; Ruitenbeek, M.; Meima, G.; Makkee, M.; Kapteijn, F.; Gascon, J. Structural and elemental influence from various MOFs on the performance of Fe@C catalysts for Fischer−Tropsch synthesis. *Faraday Discuss.* **2017**, *197*, 225−242.

(12) Kong, A.; Lin, Q.; Mao, C.; Bu, X.; Feng, P. Efficient oxygen reduction by nanocomposites of heterometallic carbide and nitrogen-enriched carbon derived from the cobalt-encapsulated indium−MOF. *Chem. Commun.* **2014**, *50*, 15619−15622.

(13) Pustovarenko, A.; Dikhtiarenko, A.; Bavykina, A.; Gevers, L.; Ramírez, A.; Russkikh, A.; Telalovic, S.; Aguilar, A.; Hazemann, J.-L.; Ould-Chikh, S.; Gascon, J. Metal−Organic Framework-Derived Synthesis of Cobalt Indium Catalysts for the Hydrogenation of CO2 to Methanol. *ACS Catal.* **2020**, *10*, 5064−5076.
(14) Xia, W.; Zhu, J.; Guo, W.; An, L.; Xia, D.; Zou, R. Well-defined carbon polyhedrons prepared from nano metal−organic frameworks for oxygen reduction. *J. Mater. Chem. A* **2014**, *2*, 11606−11613.
(15) Gates-Rector, S.; Blanton, T. The Powder Diffraction File: a quality materials characterization database. *Powder Diffr.* **2019**, *34*, 352−360.
(16) Le Bail, A.; Duroy, H.; Fourquet, J. L. Ab-initio structure determination of LiSbWO6 by X-ray powder diffraction. *Mater. Res. Bull.* **1988**, *23*, 447−452.
(17) Coelho, A. TOPAS and TOPAS-Academic: an optimization program integrating computer algebra and crystallographic objects written in C++. *J. Appl. Crystallogr.* **2018**, *51*, 210−218.
(18) Levin, I *NIST Inorganic Crystal Structure Database (ICSD)*; National Institute of Standards and Technology, (2018), (Accessed 2023-01-05)
(19) Hussain, M. Z.; Pawar, G. S.; Huang, Z.; Tahir, A. A.; Fischer, R. A.; Zhu, Y.; Xia, Y. Porous ZnO/Carbon nanocomposites derived from metal organic frameworks for highly efficient photocatalytic applications: A correlational study. *Carbon* **2019**, *146*, 348−363.
(20) Chen, B.; Ma, G.; Kong, D.; Zhu, Y.; Xia, Y. Atomically homogeneous dispersed ZnO/N-doped nanoporous carbon composites with enhanced CO2 uptake capacities and high efficient organic pollutants removal from water. *Carbon* **2015**, *95*, 113−124.
(21) Bavykina, A.; Yarulina, I.; Al Abdulghani, A. J.; Gevers, L.; Hedhili, M. N.; Miao, X.; Galilea, A. R.; Pustovarenko, A.; Dikhtiarenko, A.; Cadiau, A.; Aguilar-Tapia, A.; Hazemann, J.-L.; Kozlov, S. M.; Oud-Chikh, S.; Cavallo, L.; Gascon, J. Turning a Methanation Co Catalyst into an In−Co Methanol Producer. *ACS Catal.* **2019**, *9*, 6910−6918.
(22) Hüiter, L. J.; Stadelmaier, H. H. Über ternäre Karbide der T-Metalle Nickel, Kobalt, Eisen und Mangan mit Germanium und Indium. *Int. J. Mater. Res.* **1959**, *50*, 199−203.
(23) Baqiah, H.; Ibrahim, N. B.; Halim, S. A.; Flaifel, M. H.; Abdi, M. H. The role of cobalt doping on magnetic and optical properties of indium oxide nanostructured thin film prepared by sol−gel method. *Mater. Res. Bull.* **2015**, *63*, 147−154.
(24) Visconti, C. G.; Martinelli, M.; Falbo, L.; Infantes-Molina, A.; Lietti, L.; Forzatti, P.; Iaquaniello, G.; Palo, E.; Picutti, B.; Brignoli, F. CO2 hydrogenation to lower olefins on a high surface area K-promoted bulk Fe-catalyst. *Appl. Catal., B: Environ.* **2017**, *200*, 530−542.
(25) Wang, J.; You, Z.; Zhang, Q.; Deng, W.; Wang, Y. Synthesis of lower olefins by hydrogenation of carbon dioxide over supported iron catalysts. *Catal. Today* **2013**, *215*, 186−193.
(26) Liu, J.; Sun, Y.; Jiang, X.; Zhang, A.; Song, C.; Guo, X. Pyrolyzing ZIF-8 to N-doped porous carbon facilitated by iron and potassium for CO2 hydrogenation to value-added hydrocarbons. *J. CO2 Util.* **2018**, *25*, 120−127.
(27) Rodriguez-Gomez, A.; Ould-Chikh, S.; Castells-Gil, J.; Aguilar-Tapia, A.; Bordet, P.; Alrushaid, M. A.; Marti-Gastaldo, C.; Gascon, J. Fe-MOF Materials as Precursors for the Catalytic Dehydrogenation of Isobutane. *ACS Catal.* **2022**, *12*, 3832−3844.
(28) Ramirez, A.; Ould-Chikh, S.; Gevers, L.; Chowdhury, A. D.; Abou-Hamad, E.; Aguilar-Tapia, A.; Hazemann, J.-L.; Wehbe, N.; Al Abdulghani, A. J.; Kozlov, S. M.; Cavallo, L.; Gascon, J. Tandem Conversion of CO2 to Valuable Hydrocarbons in Highly Concentrated Potassium Iron Catalysts. *ChemCatChem* **2019**, *11*, 2879−2886.
(29) Dokania, A.; Dutta Chowdhury, A.; Ramirez, A.; Telalovic, S.; Abou-Hamad, E.; Gevers, L.; Ruiz-Martinez, J.; Gascon, J. Acidity modification of ZSM-5 for enhanced production of light olefins from CO2. *J. Catal.* **2020**, *381*, 347−354.
(30) Dang, S.; Qin, B.; Yang, Y.; Wang, H.; Cai, J.; Han, Y.; Li, S.; Gao, P.; Sun, Y. Rationally designed indium oxide catalysts for CO2 hydrogenation to methanol with high activity and selectivity. *Sci. Adv.* **2020**, *6*, No. eaaz2060.
(31) Yang, B.; Li, L.; Jia, Z.; Liu, X.; Zhang, C.; Guo, L. Comparative study of CO2 hydrogenation to methanol on cubic bixbyite-type and rhombohedral corundum-type indium oxide. *Chin. Chem. Lett.* **2020**, *31*, 2627−2633.

https://doi.org/10.1021/acscatal.2c05580
ACS Catal. 2023, 13, 1804−1811